BMC Cancer

RESEARCH

Open Access

Prognostic value of FDX1, the cuprotosis key gene, and its prediction models across imaging modalities and histology

Qiuyuan Yue[1,3†], Mingwei Zhang[2,6†], Wenying Jiang[4,5†], Lanmei Gao[7†], Rongping Ye[1,8], Jinsheng Hong[2,6*] and Yueming Li[1,8*]

Abstract

Background Cuprotosis has been identified as a novel way of cell death. The key regulator ferredoxin 1 (FDX1) was explored via pan-cancer analysis, and its prediction models were proposed across seven malignancies and two imaging modalities.

Methods The prognostic value of FDX1 was explored via 1654 cases of 33 types of cancer in the Cancer Genome Atlas database. The MRI cohort of hepatocellular carcinoma in the First Affiliated Hospital of Fujian Medical University, and CT and MRI images from the Cancer Imaging Archive, REMBRANDT and Duke databases were exploited to formulate radiomic models to predict FDX1 expression. After segmentation of volumes of interest and feature extraction, the recursive feature elimination algorithm was used to screen features, logistic regression was used to model features, immunohistochemistry staining with FDX1 antibody was performed to test the radiomic model.

Results FDX1 was found to be prognostic in various types of cancer. The area under the receiver operating characteristic curve of radiomic models to predict FDX1 expression reached 0.825 (95% CI = 0.739–0.911). Cross-tissue compatibility was confirmed in pan-cancer validation and test cohorts. Mechanistically, the radiomic score was significantly correlated with various immunosuppressive genes and gene mutations. The radiomic score was also found to be an independent prognostic factor, making it a potentially actionable biomarker in the clinical setting.

Conclusions The expression of FDX1 could be non-invasively predicted via radiomics. The radiomic patterns with biological and clinical relevance across histology and modalities could have a broad impact on a larger population of patients.

Keywords Cuprotosis, FDX1, Radiomics, Tumor microenvironment, Prognosis

†Qiuyuan Yue, Mingwei Zhang, Wenying Jiang and Lanmei Gao work and share first authorship.

*Correspondence:
Jinsheng Hong
13799375732@163.com
Yueming Li
fjmulym@163.com

Full list of author information is available at the end of the article

© The Author(s) 2024. **Open Access** This article is licensed under a Creative Commons Attribution-NonCommercial-NoDerivatives 4.0 International License, which permits any non-commercial use, sharing, distribution and reproduction in any medium or format, as long as you give appropriate credit to the original author(s) and the source, provide a link to the Creative Commons licence, and indicate if you modified the licensed material. You do not have permission under this licence to share adapted material derived from this article or parts of it. The images or other third party material in this article are included in the article's Creative Commons licence, unless indicated otherwise in a credit line to the material. If material is not included in the article's Creative Commons licence and your intended use is not permitted by statutory regulation or exceeds the permitted use, you will need to obtain permission directly from the copyright holder. To view a copy of this licence, visit http://creativecommons.org/licenses/by-nc-nd/4.0/.

Background

The global burden of cancer is increasing [1]. Currently, biomarkers for cancer are primarily assessed based on pathology. However, in addition to difficulties in obtaining specimens and its invasiveness, biopsy may also be biased, resulting in selection bias in the evaluation results. Hence, a noninvasive, convenient, and whole-lesion evaluation method is urgently needed for clinical use [2, 3]. Medical imaging meets all the three aforementioned requirements. It has become an indispensable part of cancer diagnosis and treatment and is used to evaluate macroscopic morphology, hemodynamics, and lesion metabolism [4]. Radiomics goes a step further and evaluates the microscopic molecular expression status by extracting quantitative information about the lesion and/or its surroundings. It can be used to assess gene mutations, molecular expression status, and tumor microenvironments (TME) [5]. However, current radiomic signatures have limited reproducibility and generalizability because most features are dependent on the imaging modality and tumor histology, which exhibit considerable variations [6]. Nevertheless, pan-cancer studies may help to identify commonly conserved patterns and unify biological themes across cancers.

Recent studies have identified cuprotosis as a novel way of cell death, distinct from other regulated cell death (RCD) [7]. RCD-associated genes and tumor mutational burden (TMB) are prime examples of tissue-agnostic biomarkers. Molecules involved in RCD, especially the key regulator ferredoxin 1 (FDX1), are expected to have huge potential as new biomarkers. FDX1 is an electron carrier involved in mitochondrial aerobic respiration and in the synthesis of iron-sulfur clusters, which play a key role in multiple physiological and pathological processes. Research on this biomarker is limited, and no relevant research has been conducted in radiomics.

In this study, multiple datasets and dual modalities were used to construct a radiomic model for predicting FDX1 expression. We aimed to identify the underlying radiomic features across multiple tumor phenotypes and ensure compatibility across diverse tissues and imaging contrasts.

Methods

Data source and patients

The flow of this study was depicted in Fig. 1. Transcriptome RNA sequencing data were downloaded: data on 33 cancer types from the Cancer Genome Atlas (TCGA), (https://tcga-data.nci.nih.gov/docs/publications/tcga/), non-small cell lung cancer (NSCLC) from Gene Expression Omnibus (https://www.ncbi.nlm.nih.gov/geo/query/acc.cgi?acc=GSE103584), and brain lower grade glioma (LGG) from the Chinese Glioma Genome Atlas (http://www.cgga.org.cn.portal.phpg); corresponding CT or MRI images were retrieved from the Cancer Imaging Archive, Gene Expression Omnibus, and REMBRANDT (http://caintegrator-info.nci.nih.gov/rembrandt). Duke breast cancer MRI images (https://sites.duke.edu/mazurowski/resources/breast-cancer-mri-dataset/) and clinical variables were retrieved as an independent test dataset for the prognostic value of the radiomic score.

For pan-cancer analysis, RNA sequencing data from TCGA, covering 33 types of cancer, were exploited. Corresponding clinical variables and survival outcomes were retrieved from TCGA to investigate the association

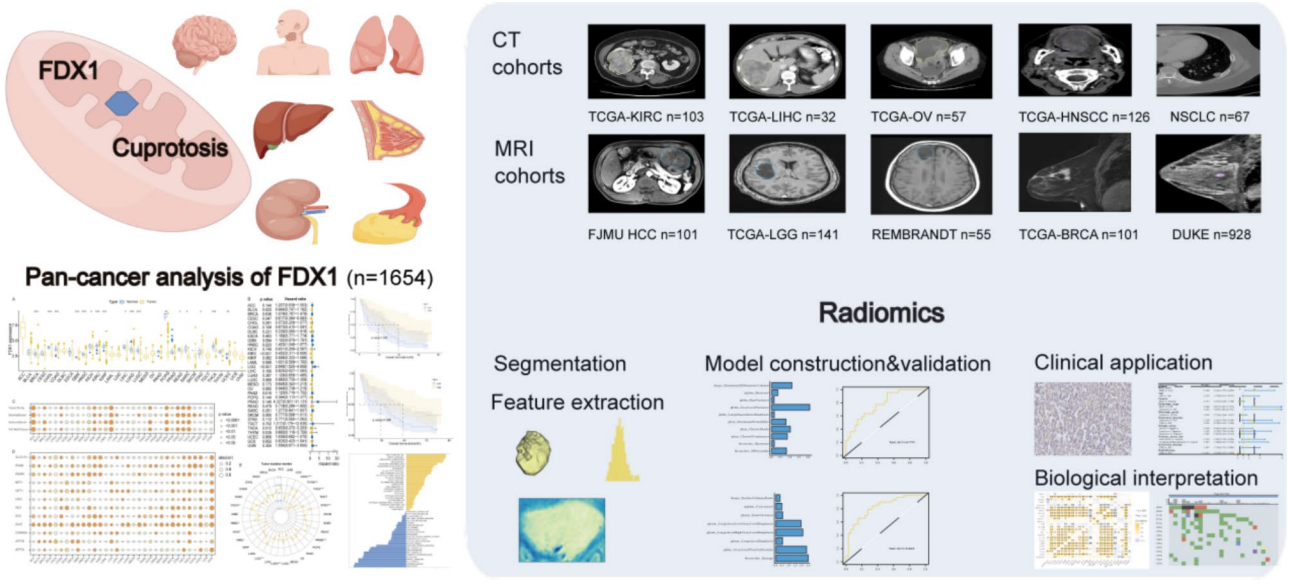

Fig. 1 The flow of this study

between FDX1 expression and overall survival (OS) across cancer types.

The inclusion criteria were as follows: (1) primary tumors, (2) complete clinical data and (3) overall survival time over 30 days. The exclusion criteria were as follows: (1) bilateral lesions and (2) cases with unknown race, histologic grade, pathologic stage.

The inclusion and exclusion criteria for the public imaging cohorts were based on the previous studies [8]. The inclusion criteria were as follows: (1) solid tumors, (2) available important clinical data, (3) survive over 30 days. The exclusion criteria were as follows:1) non-primary tumors, 2) bilateral lesions, 3) no venous phrase images for CT cohorts or contrast-enhanced images for MRI cohorts, (4) poor image quality, and (5) postoperative imaging.

The expression of FDX1 in different cell types was explored using single-cell sequencing datasets from the scTIME portal website [9]. Mutation annotation format files deposited in the TCGA data portal for somatic mutations were downloaded for analysis (https://portal.gdc.cancer.gov/).

The data of the HCC cohort diagnosed at the First Affiliated Hospital of Fujian Medical University between January 2017 and December 2020 was used to develop the MRI model. The inclusion criteria were (1) contrast-enhanced MRI images (3.0T) within 1 month before surgery; (2) complete pathological, imaging, and clinical data; and (3) good image quality. The exclusion criteria were (1) MRI images suggesting that the lesions invaded blood vessels, bile duct tumor thrombus, or extrahepatic metastasis and (2) a history of partial hepatectomy or interventional therapy. In patients with multiple lesions, the largest lesion was the preferred study object.

Preprocessing

The images were resampled to $1\times1\times1$ mm^3 pixels to eliminate the interference of inconsistent spatial resolution among the various models of imaging procedures.

VOIs segmentation

VOIs were outlined along the tumor contour by a radiologist (YQY, with >9 years of experience) under double-blind conditions and verified by another radiologist (YRP, with >6 years of experience in radiology). The entire tumor region was drawn manually using 3D Slicer software (https://download.slicer.org). During the segmentation, we made a comprehensive evaluation combined with other sequence/phase images, determined the lesion location by adjusting the appropriate window width and window position, and checked whether there were abnormal tissue masses, structural asymmetry, different density or signal, and abnormal enhancement areas to determine the tumor area.

Feature extraction

We extracted radiomic features using PyRadiomics (https://pyradiomics.readthedocs.io/en/latest/), and Z-score normalization was performed. It allowed us to derive both first-order statistics and higher-order texture features from the tumor volumes. Specifically, the extracted features included: 1) first-order statistics, which capture basic intensity values, such as mean, variance, skewness, and kurtosis; 2)shape features, which describe the geometry and size of the tumor, including metrics such as volume, surface area, and compactness; 3) texture features, derived from Gray-Level Co-occurrence Matrix (GLCM), Gray-Level Run Length Matrix (GLRLM), and Gray-Level Size Zone Matrix (GLSZM), which reflect spatial patterns and the heterogeneity of pixel intensities within the tumor.

CT radiomic model for predicting FDX1 expression

Given that the borders of the tumor in the venous phase were more distinct, features were screened on contrast enhanced KIRC CT images during the venous phase. To address the high dimensionality of the extracted features, we employed the Recursive Feature Elimination (RFE) algorithm to select the most relevant features. RFE iteratively ranks the features based on their importance in the model and removes the least significant ones. After this selection process, we reduced the number of features to 8 for the CT-based model and 13 for the MR-based model, retaining only the most relevant features for predicting FDX1 expression.

After feature selection, the remaining features were used to build the radiomic prediction model using logistic regression (LR). The selected features were input into the LR algorithm to model the probability of high vs. low FDX1 expression. This is a linear classification model where the log odds of the binary outcome are modeled as a linear combination of the selected radiomic features.

The probability of FDX1 expression predicted by the radiomic model was designated as the rad_score. To evaluate the radiomic model, ROC and precision-recall (PR) curves were plotted. The AUC and other diagnostic indices, including the BS, ACC, sensitivity, specificity, PPV, and NPV, were used to evaluate diagnostic performance. Calibration of the predictive model was demonstrated with calibration curves, and the Hosmer–Lemeshow test was used to assess the model fitness. Clinical usefulness was assessed using net benefits at different threshold probabilities determined by DCA.

We mitigated the risk of overfitting by applying RFE to select the most predictive features and ensuring a clear separation between training and test datasets. This allowed the model to generalize well to unseen data. In addition, we carefully split the datasets to ensure that the model was trained on one cohort and then validated

and tested on independent cohorts from different cancer types. This approach ensured that the model was not overfitted to the training data and could generalize well across different cancer types and imaging modalities. By separating the training, validation, and test datasets, we minimized the risk of overfitting and provided a robust evaluation of the model's performance on unseen data.

The kidney renal clear cell carcinoma (KIRC) cohort from TCGA served as the training dataset. The model was then validated using the liver hepatocellular carcinoma (LIHC) cohort from TCGA. The purpose of the validation was to fine-tune the model and evaluate its performance on an independent dataset from a different cancer type. To assess the generalizability of the model, it was tested on additional external cohorts, including the OV (ovarian cancer), HNSCC (head and neck squamous cell carcinoma), and NSCLC cohorts from TCGA. These test datasets provided a robust evaluation of the model's performance across different cancer types and ensured that the model could generalize well to unseen data.

MR radiomic model for predicting FDX1 expression

The MRI procedure for the hospital HCC cohort was as follows: T1C sequence after contrast agent injection was used for analysis, which had clearer comprehension of the anatomy. All MRI images were corrected using the N4 bias field correction algorithm, a popular method for correcting low-frequency intensity non-uniformity present in MRI image data, known as bias. The model was constructed using AP T1C images of the hospital HCC cohort. Then, the RFE algorithm was used to screen features, LR algorithm was used to model features, and rad_score was constructed to predict the expression level of FDX1. The model evaluation index was the same as that of the CT model. The model was verified using the TCGA-LGG cohort to check its performance on an independent dataset from a different cancer type. Finally, the model was tested on the REMBRANDT cohort (glioma dataset) and the Duke breast cancer cohort to evaluate its ability to generalize across additional cancer types and imaging modalities.

According to the exclusion criteria (poor image quality and postoperative imaging), 52 OV patients, 60 HNSCC patients, 104 NSCLC patients, 36 LIHC patients, 11 REMBRANDT patients, 29 BRCA patients, zero Duke patients were eliminated from patients with images.

IHC

HCC tissues from the First Affiliated Hospital of Fujian Medical University were fixed, embedded in paraffin, and sectioned for IHC staining by an FDX1 antibody (Abmart, Shanghai, China). IHC was performed with antibodies targeting FDX1 (dilution 1:100), determined based on preliminary optimization experiments to ensure specific and robust staining. The stained tissue sections were counterstained with hematoxylin. Secondary biotinylated antibodies specific to the species of the primary antibody were used, followed by a horseradish peroxidase (HRP)-conjugated streptavidin for signal amplification.

Staining Protocol was as follows: Formalin-fixed, paraffin-embedded (FFPE) tissue sections from the HCC cohort were used for IHC. Tissue sections were cut at 4 μm thickness and mounted on glass slides. The tissue sections were deparaffinized using xylene and rehydrated through graded alcohols.

Antigen retrieval was performed using a citrate buffer (pH 6.0) at 95 °C for 20 min to enhance the accessibility of the FDX1 epitopes. Endogenous peroxidase activity was blocked with 3% hydrogen peroxide for 10 min at room temperature. Tissue sections were incubated with the FDX1 primary antibody (1:100 dilution) overnight at 4 °C. The sections were then incubated with a species-specific biotinylated secondary antibody for 30 min at room temperature, followed by the HRP-conjugated streptavidin for 15 min. The signal was developed using a diaminobenzidine (DAB) substrate, resulting in a brown color for positive staining. The sections were counterstained with hematoxylin for contrast.

AIPATHWELL (Wuhan Servicebio Technology Co.), serves as a sophisticated tool for the comprehensive panoramic assessment of FDX1 IHC stained Sect. [10]. H-Score were calculated as (percentage of weak intensity*1) +(percentage of moderate intensity*2) +(percentage of strong intensity*3) [11]. Then H-Scores were categorized as low or high for further statistical analysis, based on the median cut-off.

Quantification and statistical analysis

Normally and non-normally distributed quantitative data are presented as mean ± standard deviation and median (interquartile range), respectively, whereas categorical data are shown as percentages. The Wilcoxon rank-sum test was used to compare differences in quantitative data between the groups, whereas the chi-square and Fisher exact tests were used to compare differences in categorical variables between the groups.

All qualified cases were divided into two groups according to high and low FDX1 expression levels separated by the median value. Spearman or Pearson correlation coefficients were calculated using correlation analysis. Survival analysis was performed using Kaplan-Meier curves to compare the OS between high and low expression groups, and the log-rank test was used for significance testing. Univariate and multivariate Cox regression were applied to identify the hazard ratio (HR) of FDX1 expression in each cancer type. The prognostic significance of FDX1 was visualized through forest plots, depicting the hazard ratios. To identify differentially enriched pathways

between FDX1^{high} and FDX1^{low} groups, gene set variation analysis was employed to calculate enrichment scores for the 50 hallmark pathways from the molecular signature database (MSigDB version 6.0).

Both immune and stromal scores were calculated using R packages "limma" and "estimate." The correlation of FDX1 expression level with TMB was conducted via the R package "fmsb." The rad_score was calculated, and patients were dichotomized by the R package "survMisc" for survival and correlation analysis. To compare the mutation differences between the high- and low-rad_score groups, visualizations of the highest frequency of mutations were performed in R using the maftools package. Each point on the x-axis of the waterfall plot represents an individual patient, used to calculate mutation frequency and quickly identify genes with high mutation frequencies in the sample.

The statistical significance level was set at a P-value (two-tailed) of <0.05, except when specifically stated.

Results

Pan-cancer analysis

FDX1 expression was significantly lower in tumor tissues than in normal tissues ($P<0.05$; Fig. 2A). As depicted in Fig. 2B, the FDX1 expression level was significantly associated with OS in patients with various cancers. The TME score was significantly correlated with the FDX1 expression level (Fig. 2C). Various cuprotosis-related genes were also significantly correlated with FDX1 expression

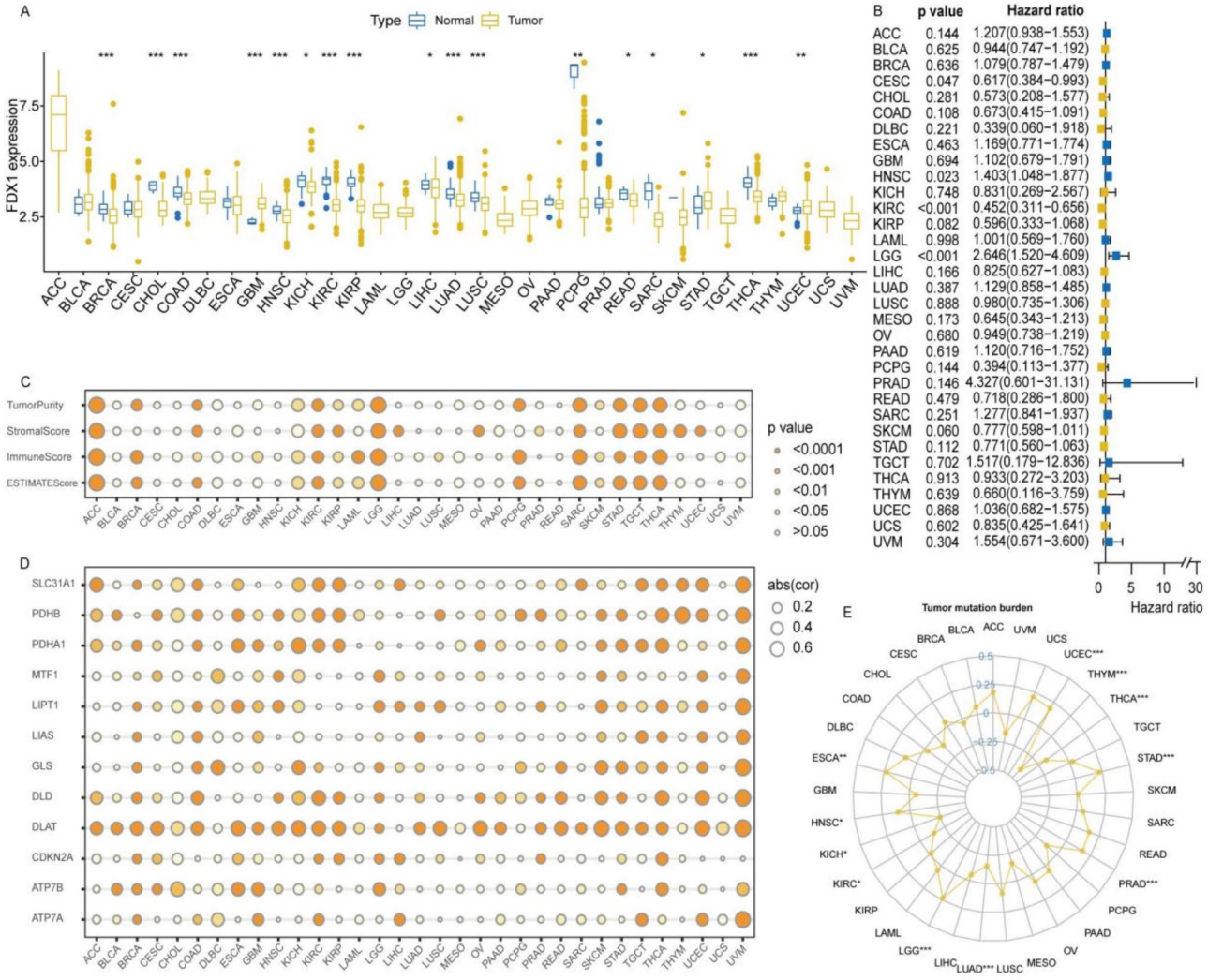

Fig. 2 Pan-cancer analysis of the significance of FDX1 in various cancer types. (**A**) Comparison of FDX1 expression levels across 33 cancer types, highlighting potential differences in expression patterns. (**B**) Cox regression analysis of overall survival to evaluate the prognostic significance of FDX1 across multiple cancers. (**C**) Correlation analysis between FDX1 expression and tumor microenvironment scores, exploring the impact of FDX1 on immune infiltration and the TME. (**D**) Analysis of FDX1's relationship with cuprotosis-related genes, identifying FDX1's role in copper-induced cell death. (**E**) Correlation between FDX1 expression and tumor mutational burden, exploring FDX1's influence on genomic instability in different cancer types

(Fig. 2D). TMBs in LGG and KIRC were significantly correlated with FDX1 expression (Fig. 2E).

In the programmed cell death protein 1 (PD1) immunotherapy cohort of the KIRC cohort (Table S1), there was a significant difference in OS between the FDX1 high and low expression groups (P=0.036) (Fig. 3A). FDX1 expression was an independent predictor of OS (hazard ratio [HR], 0.697; 95% CI=0.558–0.869) (Fig. 3B). General distributions of FDX1 expression across multiple cell types were manifested in Fig. 3C and D. Differentially expressed genes between the high and low expression groups of FDX1 were enriched in oxidative phosphorylation, fatty acid metabolism, IL-2/STAT5 signaling and IL-6/JAK-STAT3 signaling pathways (Fig. 3E).

In the LIHC cohort (Table S2), univariate Cox regression analysis showed that high FDX1 expression was significantly correlated with OS in patients with LIHC (HR 0.685, 95% CI=0.513–0.906 (Fig. 4A). General distributions of FDX1 expression across multiple cell types were manifested in Fig. 4B and C. Differentially expressed genes between the high and low expression groups of FDX1 were enriched in multiple pathways, also including oxidative phosphorylation, IL-2/STAT5 signaling and IL-6/JAK-STAT3 signaling pathways (Fig. 4D).

In the Cancer Genome Atlas Low Grade Glioma Collection (TCGA_LGG) cohort (Table S3), univariate Cox regression analysis showed that high expression of FDX1 was significantly associated with OS in patients with LGG (Fig. 5A). General distributions of FDX1 expression across multiple cell types were manifested in Fig. 5B and C. Differentially expressed genes between the high and low expression groups of FDX1 were enriched in multiple pathways, also including oxidative phosphorylation, fatty acid metabolism, IL-2/STAT5 signaling and IL-6/JAK-STAT3 signaling pathways (Fig. 5D). In the Chinese Glioma Genome Atlas Low Grade Glioma Collection (CCGA_LGG) cohort (Table S4), high expression of FDX1 was also an independent risk factor (Fig. 5E). Differentially expressed genes between the high and low FDX1 expression groups are depicted in Fig. S1, including oxidative phosphorylation, IL-2/STAT5 signaling and IL-6/JAK-STAT3 signaling pathways.

CT radiomic model to predict FDX1 expression

Initially, we extracted 107 radiomic features per imaging modality across the tumor regions. Finally, eight features were screened and entered the logistic regression (LR) model; the weight coefficients of each feature are listed in Table S5. The accuracy (ACC), sensitivity, specificity, negative predictive value (NPV), positive predictive value (PPV), and Brier score (BS) were 0.767, 0.786, 0.727, 0.615, 0.859, and 0.155, respectively. The area under the receiver operating characteristic curve (AUROC) was 0.825 (95% CI=0.739–0.911, Fig. 6A), and the calibration and decision curves demonstrated good calibration and clinical benefit (Fig. 6B and C). The LIHC cohort was used as the validation set, and the ACC, sensitivity, specificity, NPV, PPV, and BS were 0.788, 0.947, 0.571, 0.75, 0.889, and 0.191, respectively. The AUROC was 0.748 (95% CI=0.568–0.929, Fig. 6D), and the calibration curves and decision curves demonstrated good calibration and clinical benefit (Fig. 6E and F). To confirm the cross-tissue compatibility that this study sought to harness using the radiomic platform, the prediction model was tested in the ovarian cancer (OV), head and neck squamous cell carcinoma (HNSCC), and non-small cell lung cancer (NSCLC) cohorts. The AUROCs were 0.779 (95% CI=0.660–0.899), 0.738 (95% CI=0.607–0.869), and 0.805 (95% CI=0.680–0.931), respectively (Fig. 6G, J, and M). All calibration and decision curves demonstrated good calibration and clinical benefit (Fig. 6H, I, K, L, N and O).

MR radiomic model for predicting FDX1 expression

The recursive feature elimination (RFE) algorithm screened out 13 features from initial 107 radiomic features extracted, whose coefficients in the LR model are shown in Table S6. The ACC, sensitivity, specificity, NPV, PPV, and BS were 0.693, 0.51, 0.88, 0.638, 0.812, and 0.21, respectively. The AUROC was 0.717 (95% CI=0.617–0.816, Fig. 7A). The calibration and decision curves demonstrated good calibration and clinical benefit (Fig. 7B and C). As validation in the TCGA_LGG cohort, the ACC, sensitivity, specificity, NPV, PPV, and BS were 0.709, 0.529, 0.887, 0.656, 0.822, and 0.206, respectively. The AUROC was 0.737 (95% CI=0.653–0.821, Fig. 7D). Similarly, the prediction model was tested using the Repository of Molecular Brain Neoplasia Data (REMBRANDT) and TCGA breast cancer (BRCA) cohorts; the AUROCs were 0.763 (95% CI=0.637–0.889) and 0.742 (95% CI=0.620–0.863), respectively (Fig. 7G and J). All calibration and decision curves demonstrated good calibration and clinical benefit, respectively (Fig. 7E, F, H, I, K, and L).

Clinical application of the radiomic score (rad_score)

For further evidence of the application of the rad_score, immunohistochemistry (IHC) of FDX1 between the high- and low-rad_score specimens are shown in Fig. 8.

Significant differences were observed between the groups. In the KIRC, HNSCC, LGG, and Duke cohorts, the rad_score was identified as an independent predictor of patients' OS (P=0.008, 0.006, 0.013, and 0.010, respectively) (Fig. 9).

Biological correlation analysis of the rad_score

In the KIRC, HNSCC, TCGA_LGG, and BRCA cohorts, the rad_score was significantly correlated with the

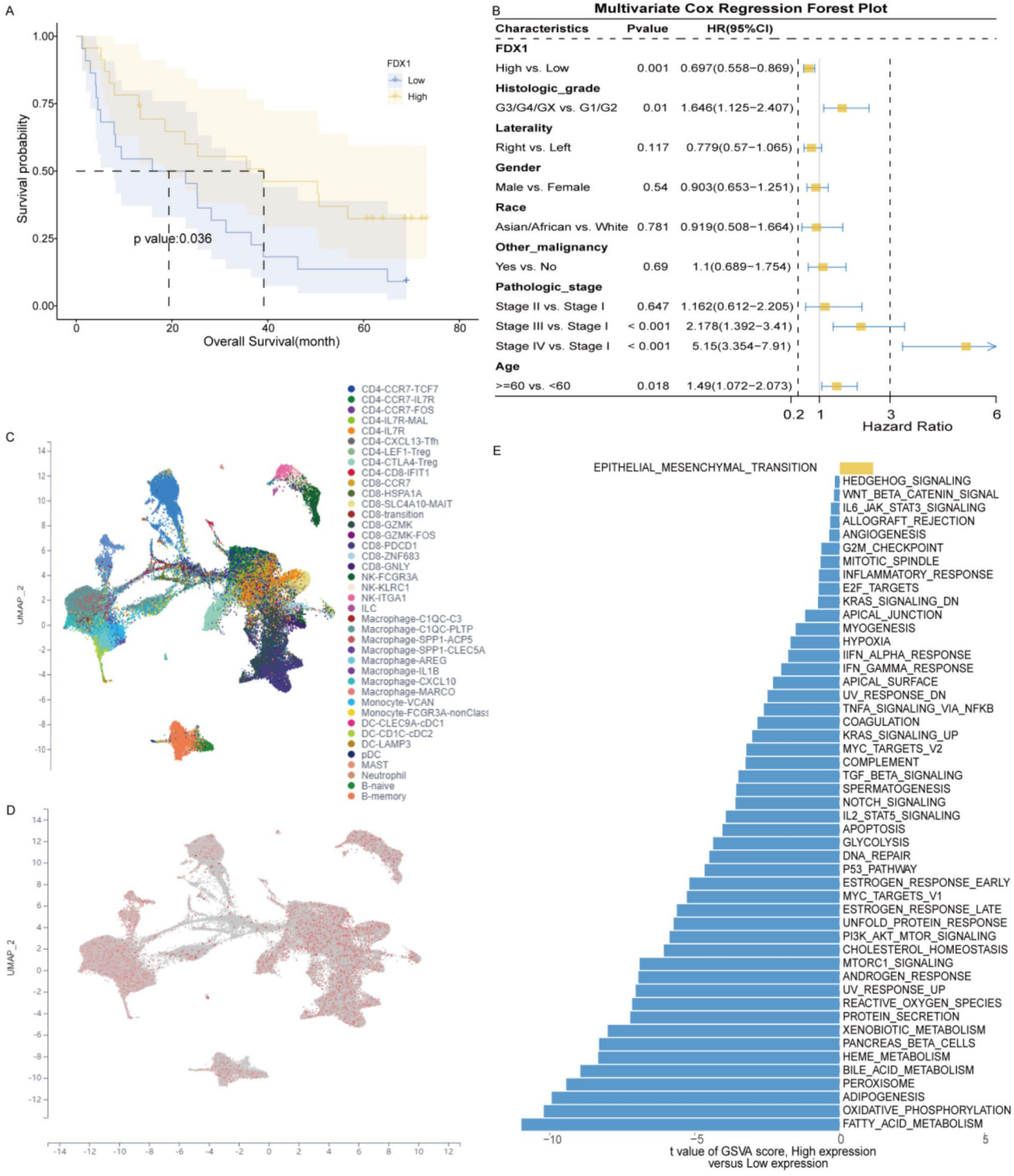

Fig. 3 Data mining in the KIRC cohort to assess the prognostic role of FDX1 in kidney renal clear cell carcinoma. (**A**) Kaplan-Meier curve showing the difference in OS between high and low FDX1 expression groups. (**B**) Cox regression analysis of OS in the KIRC cohort to determine the prognostic impact of FDX1. (**C**) FDX1 expression across different cell types in KIRC, illustrating its cellular distribution. (**D**) Heatmap of FDX1 expression values, categorized by high and low expression groups. (**E**) Gene set variation analysis of pathways enriched between FDX1 high and low expression groups

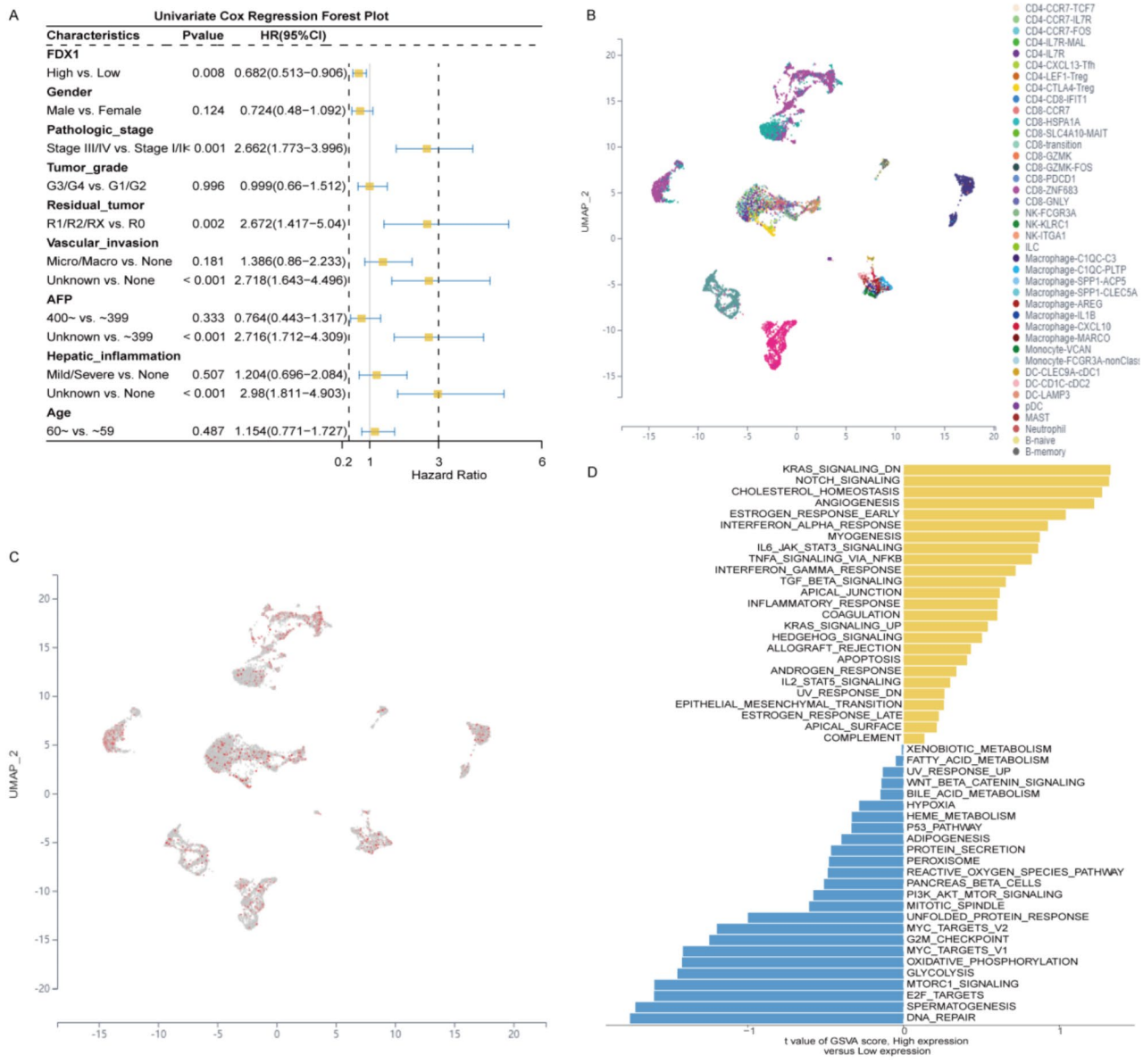

Fig. 4 Data mining in the LIHC cohort to evaluate FDX1's prognostic significance in liver hepatocellular carcinoma. (**A**) Cox regression analysis of overall survival to assess FDX1's impact on survival in the LIHC cohort. (**B**) Distribution of FDX1 expression across different cell types in LIHC, illustrating its expression pattern. (**C**) Heatmap of FDX1 expression values, categorized by cell type. (**D**) GSVA revealing the pathways enriched in FDX1 high and low expression groups, exploring FDX1's biological role in liver cancer

expression levels of inhibitory immune genes (Figs. S2–6). Like the broad cross-tissue compatibility of the radiomic model, some common ground was found among different histology, such as lymphocyte activation gene-3. In the KIRC, LIHC, OV, HNSCC, TCGA_LGG, and BRCA cohorts, significantly different mutation rates were observed between patients with high and low rad_scores, most of which were missense mutations (Figs. 10A–C and S7–9). In addition, common features among different histology were identified, such as mutations in the phosphatidylinositol 3-kinase (PI3K)/AKT/mammalian target of rapamycin pathway and C3.

Discussion

The hallmarks of cancer connect all types of cancer cells at the cellular phenotype level, [12] including resistance to cell death, remodeling of cellular metabolism, and immune escape. The TME plays an integral role in tumorigenesis. Feedback loops can be formed between RCD and the TME, and targeting RCD provides new intervention strategies and targets for cancer therapy. Cuprotosis is a recently identified form of RCD [7]. As a key regulator, FDX1 is expected to have significant potential as a biomarker in oncology. In the present study, we found that (1) FDX1 is closely related to the prognosis of

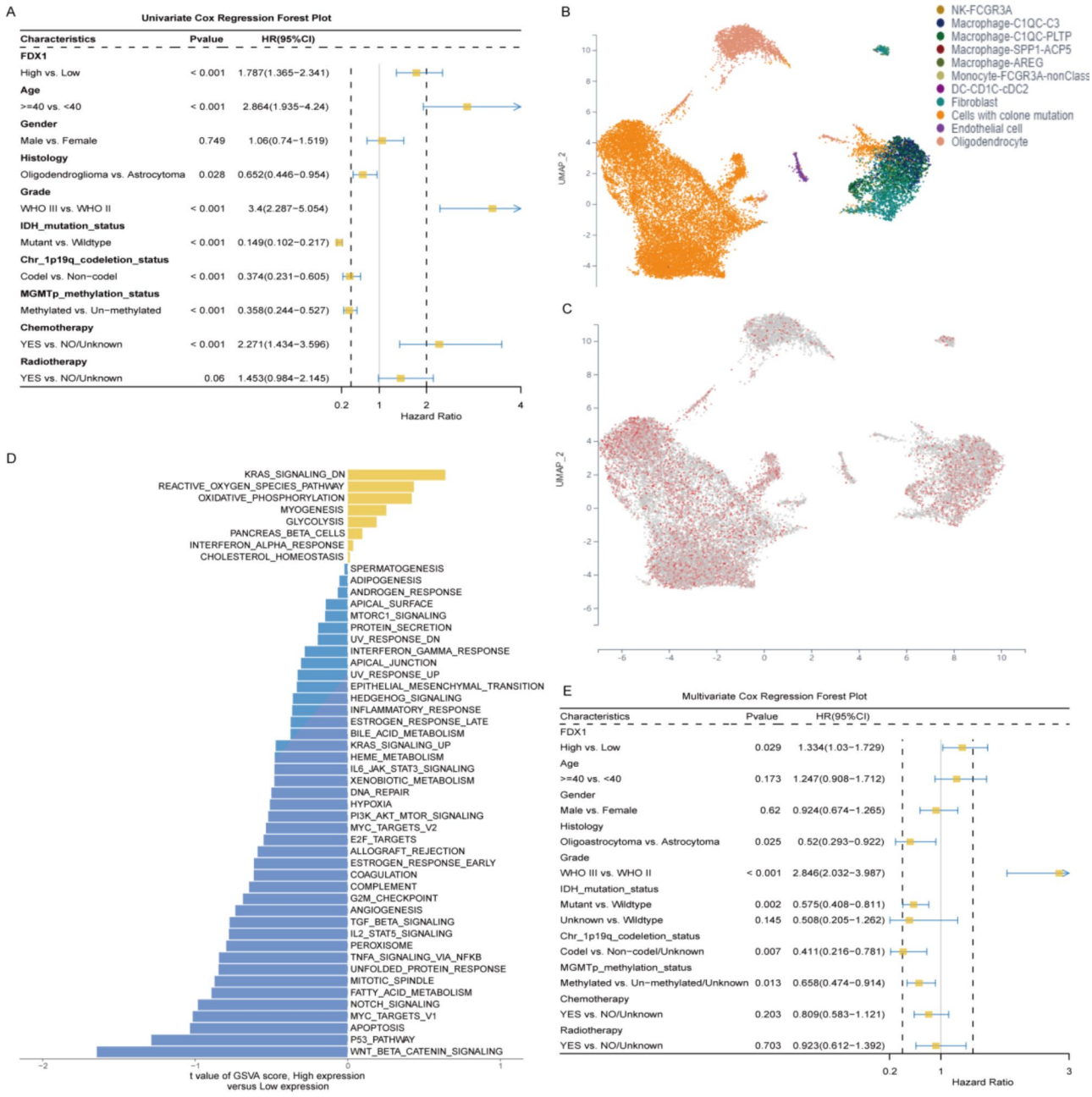

Fig. 5 Data mining in the LGG cohort to evaluate the prognostic role of FDX1 in lower-grade glioma. (**A**) Cox regression analysis of overall survival in the TCGA-LGG cohort, assessing FDX1's prognostic value. (**B**) FDX1 expression across different cell types in LGG, indicating the cellular distribution. (**C**) Heatmap of FDX1 expression values across different cell types in LGG. (**D**) GSVA of pathways enriched in FDX1 high and low expression groups in the LGG cohort. (**E**) Cox regression analysis of overall survival in the CCGA-LGG cohort to further validate FDX1's prognostic role

various cancers; (2) radiomics based on CT could non-invasively predict FDX1 expression across cancer histology, with an AUROC reaching 0.825; (3) the area under the curve (AUC) of radiomic prediction receiver operating characteristic (ROC) curves based on T1 contrast-enhanced (T1C) MRI was 0.763 for FDX1 expression across cancer types; and (4) rad_scores were associated with immune checkpoints, gene mutations, and patient prognosis.

FDX1 is in the mitochondrial matrix and is closely associated with mitochondrial metabolism through the transferring of electron chains [7]. FDX1 regulates the lipid metabolism and phosphorylation, increases the levels of interleukin-2 and interferon-, and boosts the anti-tumor immunity in certain circumstances. However,

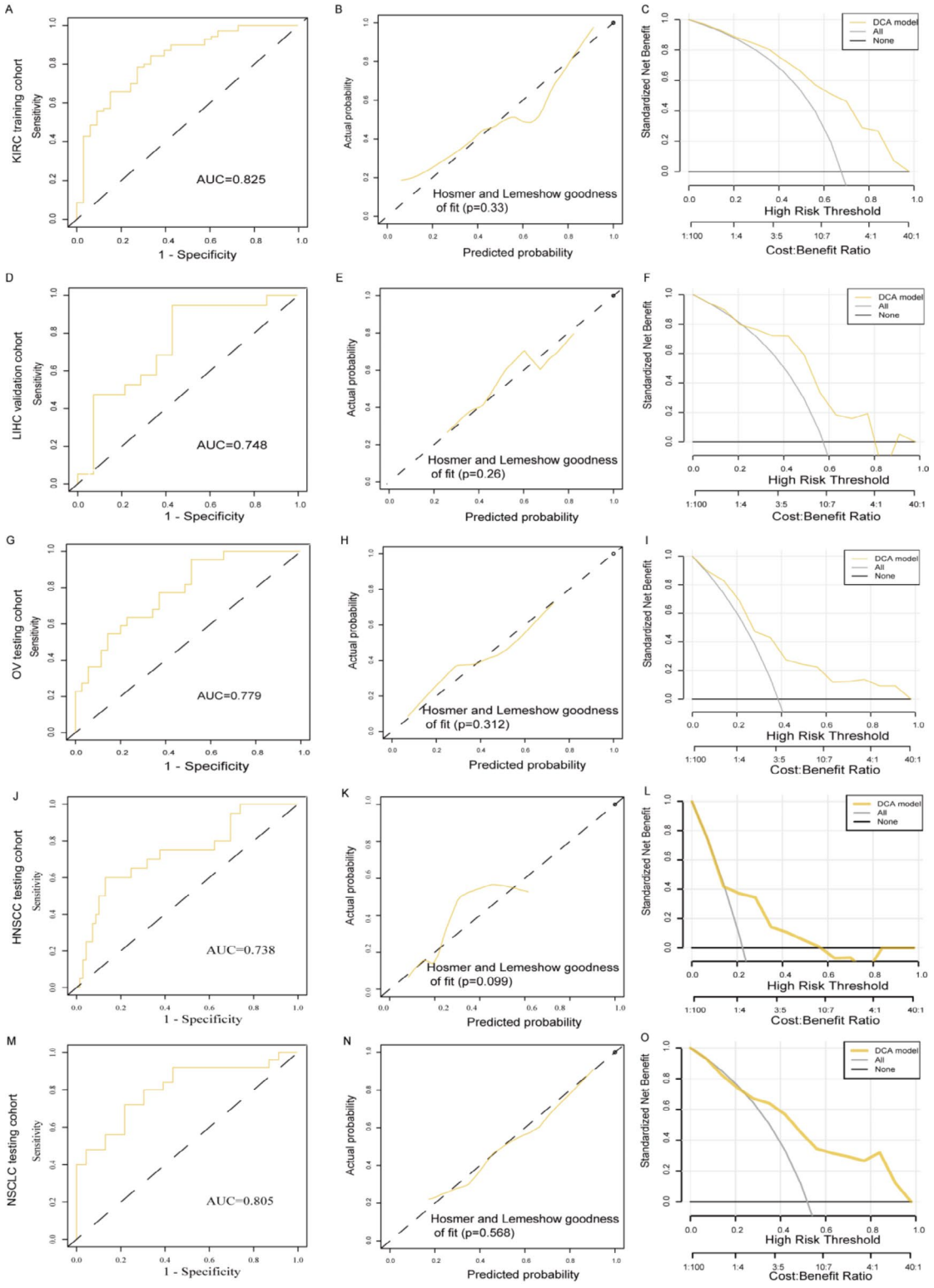

Fig. 6 Evaluation and validation of the CT-based radiomic model for predicting FDX1 expression across multiple cancer types. (**A**-**C**) Performance evaluation in the KIRC training cohort, using the ROC curve, calibration curve, and decision curve analysis to assess model accuracy. (**D**-**F**) Validation of the radiomic model in the LIHC cohort, with performance metrics including ROC, calibration, and decision curve analysis. (**G**-**I**) Testing of the model in the OV cohort, showing the generalizability of the model. (**J**-**L**) Performance metrics for the HNSCC cohort, including ROC, calibration, and decision curve analysis. (**M**-**O**) Testing of the model in the NSCLC cohort, with corresponding performance metrics

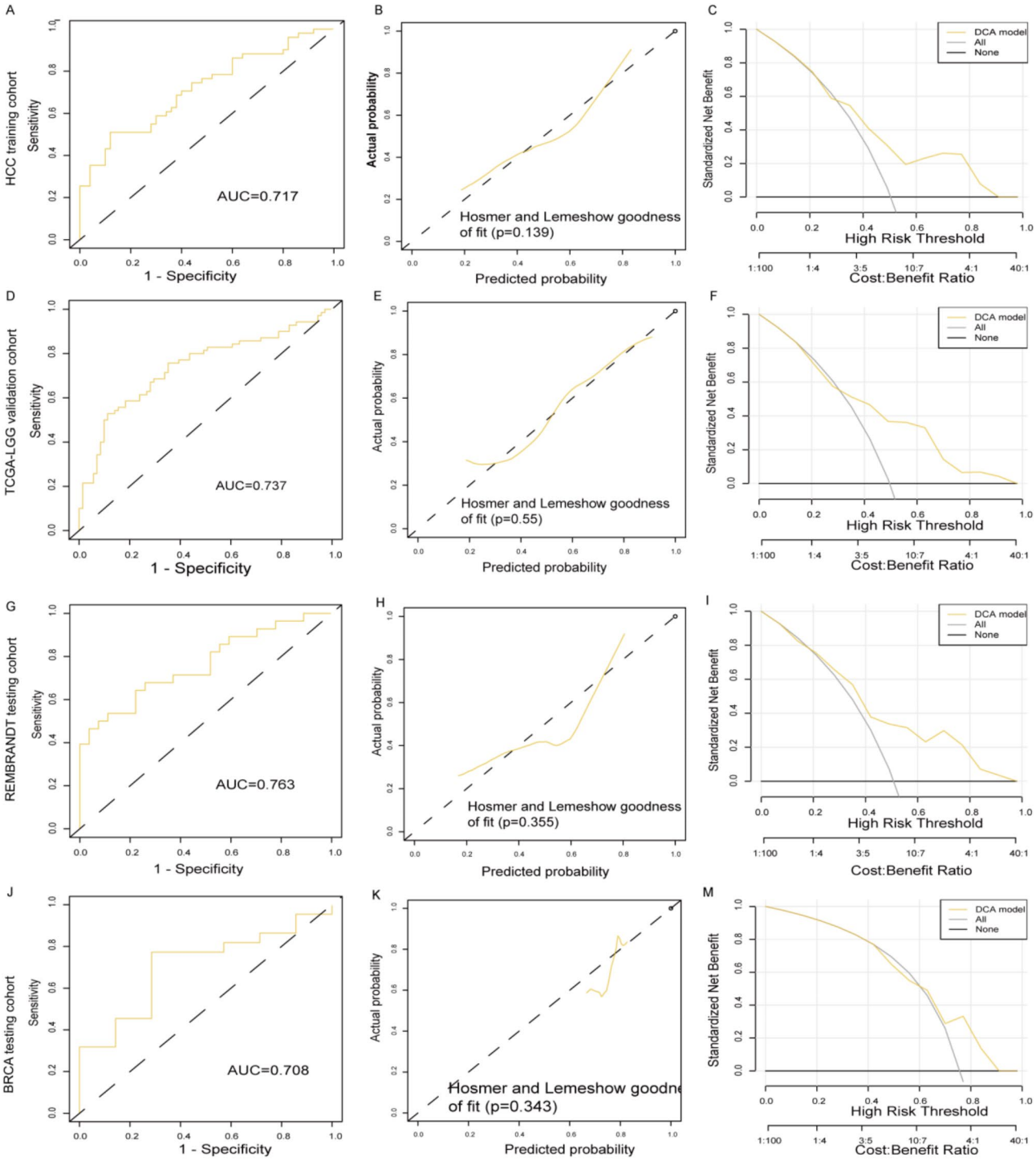

Fig. 7 Evaluation and validation of the MRI-based radiomic model for predicting FDX1 expression in different cancer types. (**A**-**C**) Performance of the radiomic model in the HCC cohort (training set), including ROC curve, calibration curve, and decision curve analysis. (**D**-**F**) Validation of the MRI-based model in the TCGA-LGG cohort. (**H**-**J**) Testing the model in the REMBRANDT cohort, showing its ability to generalize across different cancers. (**K**-**M**) Evaluation of the model's performance in the BRCA cohort, including ROC, calibration, and decision curve analysis

FDX1 may contribute to immunosuppressive TME via copy number variation events. As immune-directed therapies rapidly reshape the landscape of clinical oncology, FDX1 has been reported to be a potential predictor of response to immunotherapy. For example, FDX1 is a source of genetic variation and is a potential prognostic factor for KIRC [13]. According to our findings, FDX1 expression is correlated with TMB in several types of

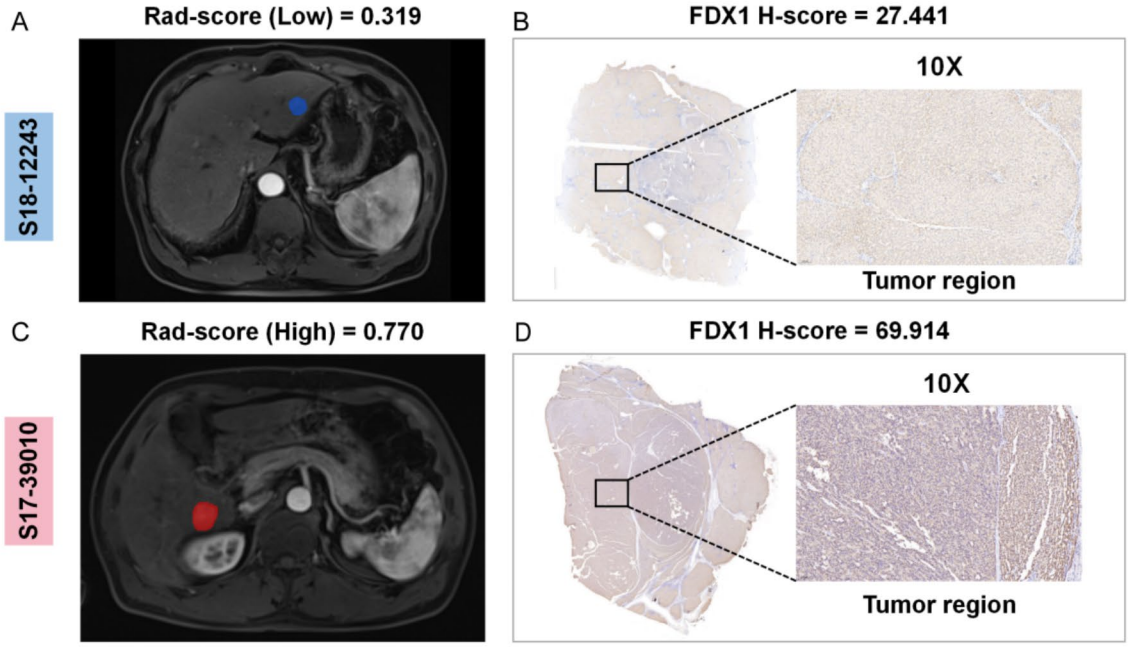

Fig. 8 Immunohistochemistry staining of FDX1 in high and low rad_score specimens: (A and B) a representative MRI image with high rad_score and its corresponding immunohistochemistry staining of FDX1; (C and D) a representative MRI image with low rad_score and its corresponding immunohistochemistry staining of FDX1

cancers. Previous studies have shown that the trigonometric relationship among oncogene signaling pathways, immunosuppressive networks, and metabolic remodeling affects cancer immunogenicity and immunotherapeutic effects. FDX1 promotes adenosine tri-phosphate production and regulates metabolism in the TME. In addition to lung cancer, [14] we found that FDX1 is prognostic in various types of cancer and could serve as a biomarker for cancers across histology. TME and specific genetic mutations in different cancers can influence how cuprotosis is regulated. This variability in the TME and genetic context likely contributes to the differences observed in the pan-cancer analysis. Tumors with metabolic reprogramming that heavily relies on mitochondrial function, like KIRC, are more likely to be affected by FDX1 expression, potentially explaining why FDX1 shows a stronger prognostic impact in these cancers [15].

The enriched pathways are crucial in shaping the metabolic environment of tumor cells, which in turn can influence tumor progression, metastasis, and response to therapies [16]. Tumor cells often undergo metabolic reprogramming to sustain rapid growth, and FDX1's involvement in mitochondrial function suggests it may play a broader role in cancer cell metabolism and survival [15]. Also, FDX1 is related to immune-associated pathways, such as the IL-2/STAT5 and IL-6/JAK-STAT3 signaling pathways, both of which are crucial for T cell activation. Given the growing body of literature linking metabolism and immunity, as well as mitochondria and immune responses, we believe that FDX1 may indeed have an important role in immune regulation [17].

Yet, the current assessment of biomarkers is based on pathological examinations, which are unsuitable for in vivo dynamic monitoring. Genomic instability enables the plasticity of tumor phenotypes, [12] which demands dynamic monitoring. Hence, some researchers have resorted to radiomics and assessed genomic mutations, molecular expression status, and TME by extracting quantitative information from the lesion and/or its surroundings [18–21]. Here, we formulated a noninvasive prediction of FDX1 status across histological and imaging modalities, with an AUROC of 0.825. Likewise, the discrimination of CT-based radiomics to predict epidermal growth factor receptor mutations in lung cancer reached 0.85, [22] and the AUROC of MRI-based radiomics to predict the positive rate of Ki67 in nasopharyngeal carcinoma reached 0.85 [23]. Zhang et al. used CT-based radiomics to predict Ki67 levels in gastrointestinal stromal tumors [24]. A fully automated CT model was constructed to predict mutations in isocitrate dehydrogenase (IDH) gliomas [25].

Most importantly, we discovered unifying radiomic phenotypes that are conserved across multiple cancer types and imaging modalities, which could have a

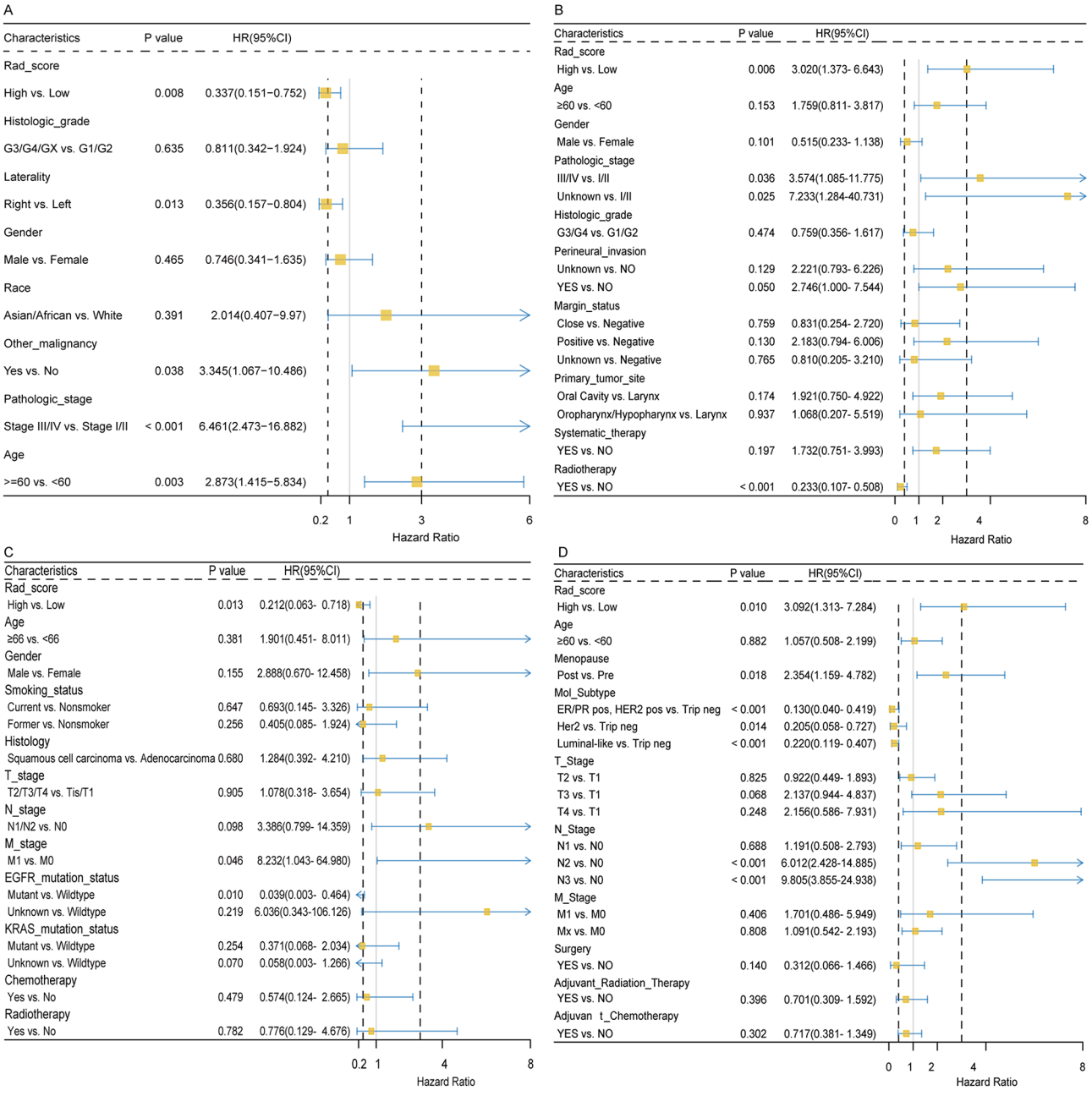

Fig. 9 Cox regression analysis of overall survival based on radiomic scores in various cancer types. (**A**) KIRC cohort, (**B**) HNSCC cohort, (**C**) NSCLC cohort, and (**D**) BRCA cohort, illustrating the prognostic significance of the radiomic scores across these cancer types

broad impact on a larger population of patients. Current radiomic signatures have limited reproducibility and generalizability because most features are dependent on the imaging modality and tumor histology, making them sensitive to variations in the scan protocol [18]. Pan-cancer studies may help to identify commonly conserved patterns and unify biological themes across cancers. TMB is a prime example of a tissue-agnostic biomarker used to select patients for specific treatment regardless of tumor histology. The lack of standardization and diverse tissue contrasts in different modalities has hampered pan-cancer studies. Several international multi-institutional studies have reported efforts in the context of radiological imaging [26]. For instance, four unifying imaging subtypes across three malignancies and two major imaging modalities have been proposed [27]. These tumor subtypes demonstrate distinct molecular characteristics and prognoses after conventional therapies. Our analysis indicated common cross-tissue compatibility of radiomic features. Thus, this study provides a conceptual framework that allows for the aggregation of datasets with disparate modalities and cancer types,

Fig. 10 Analysis of differential mutation patterns between high and low rad_score groups. (**A**) Mutation analysis in the OV cohort, (**B**) LGG cohort, (**C**) BRCA cohort, identifying key mutations associated with high and low radiomic scores across these cancers

similar to the integration of molecular data in pan-cancer studies using TCGA.

Despite the good performance, there is still room for improvement. According to previous studies, combining different phases in CT and multiple magnetic resonance sequences may further improve prediction. In advanced rectal cancer, the discrimination of the effect prediction of neoadjuvant chemotherapy by multimodal radiomics was as high as 0.93, compared with 0.859 for the T2-weighted imaging model, 0.828 for the apparent diffusion coefficient (ADC) model, 0.812 for the dynamic contrast-enhanced T1 model, and 0.766 for the CT model [25]. In addition to the modality, a multiregional radiomic model may further improve the performance of the models. As indicated by the single-cell sequencing results, FDX1-expressing cells were widely distributed. Previous studies have demonstrated the advantages of multi-region models. In addition to the tumor region, peritumoral features are significantly associated with the efficacy of targeted therapy in breast cancer [28]. When

predicting IDH mutation status in gliomas, the AUROC of the multi-region model reached 0.96, whereas the maximum area under the curve of the single-region model was 0.88 [29].

Moreover, our study found that radiomic models were related to disease prognosis. Thus, they may be used for the risk stratification of patients with cancer. The CT-based radiomic model constructed by Roger Sun could similarly predict tumor infiltration lymphocytes (TIL) in solid tumors and the efficacy of anti-PD1 and programmed cell death ligand 1 [30]. MRI-based radiomic markers can be used to calculate the recurrence risk in patients with breast cancer [31]. Radiomic prediction outperformed clinical and genomic models in patients with lung cancer.

Driven by data, radiomics often lacks interpretability. Most studies have failed to explore the relationship between imaging features and underlying biological processes. Given that radiological changes are believed to be driven by genomic alterations, the same situation also applies to -omics, that is, radiomics. In this study, rad_scores were significantly correlated with suppressive immune molecules. Owing to aberrant genetic alterations, the gain-of-function of proto-oncogenes or the loss-of-function of tumor suppressor genes are the dominant driving forces underlying tumorigenesis. We compared the mutation frequencies between the high and low rad_score groups and found significant differences in various genes, such as phosphatase and tensin homolog deleted on chromosome 10 (PTEN) and PI3K. As reported by other studies, dysregulation of the PI3K/AKT pathway occurs frequently in cancer and can lead to metabolic reprogramming; additionally, the loss of PTEN can promote cancer. These results provide a molecular explanation for our radiomic models. Similarly, Bao et al. found that contrast-enhanced ultrasound imaging could predict changes in the expression of apoptotic molecules in liver metastases [32]. Grossmann found that MRI radiomics could predict changes in apoptosis and immune response-related pathways in glioblastoma [33]. In head and neck squamous cell carcinoma, radiomics could identify molecular expression and the TME [34].

Limitation of the study

First, the image acquisition equipment and sequences in the public database were homogeneous; hence, further verification using a standardized prospective cohort is required. Secondly, the inclusion of cancer types was limited. Therefore, future studies should expand the number of diseases and sample sizes and evaluate the generalization ability of the model. Combining multiple imaging phrases, modals, and volumes of interest (VOIs) may further improve prediction. Meanwhile, the lack of expression difference and significant OS association does not preclude FDX1 from being involved in other aspects of tumor biology, such as metabolic reprogramming or immune response modulation, which could be crucial in understanding the tumor microenvironment. Thirdly, while it is indeed economical, there are limitations of relying solely on public scRNA sequencing data, and caution against drawing strong conclusions about selective expression based on these results. Such data may not always capture the full complexity of gene expression across different tumor microenvironments. Further studies with more targeted experimental validation (e.g., flow cytometry or immunohistochemistry) would be necessary to accurately determine FDX1 expression in specific cell populations.

Conclusions

In conclusion, FDX1 expression is a prognostic marker for patients with cancer and can be estimated using radiomic models across imaging modalities and histology. The rad_score is interpretable and has the potential to become a clinically actionable biomarker.

Abbreviations

ACC	Accuracy
AP	Arterial Phase
AUC	Area Under the Curve
BS	Brier Score
CGGA	Chinese Glioma Genome Atlas
DCA	Decision Curve Analysis
DSS	Disease Specific Survival
FDX1	Ferredoxin 1
GSVA	Gene Set Variation Analysis
HCC	Hepatocellular Carcinoma
IHC	Immunohistochemical
ISC	Iron-Sulfur Clusters
IQR	Interquartile Range
KIRC	Kidney Renal Clear Cell Carcinoma
LGG	Lower Grade Glioma
LIHC	Liver Hepatocellular Carcinoma
LR	Logistic Regression
MSI	Microsatellite Instability
NPV	Negative Predictive Value
OS	Overall Survival
OV	Ovary Cancer
PPV	Positive Predictive Value
PR	Precision Recall
RCD	Regulated Cell Death
REMBRANDT	The Repository Of Molecular Brain Neoplasia Data
RFE	Recursive Feature Elimination
ROC	Receiver Operating Characteristic
SD	Standard Deviation
T1C	T1 post-gadolinium
TCGA	The Cancer Genome Atlas
TCIA	The Cancer Imaging Archive
TIL	Tumor Infiltration Lymphocytes
TMB	Tumor Mutational Burden
TME	Tumor Microenvironment
VOIs	Volumes Of Interest
VP	Venous Phase

Supplementary Information

The online version contains supplementary material available at https://doi.org/10.1186/s12885-024-13149-x.

Supplementary Material 1

Supplementary Material 2

Acknowledgements
We thank Figdraw (https://www.figdraw.com/static/index.html#/) for the elements employed in the graphic abstract.

Author contributions
JH and YL conceived and supervised the study. QY and MZ designed and conducted the experiments. QY collected the data and delineated VOIs. WJ authored the manuscript. LG analyzed the data. RY contributed to VOI segmentation. All authors reviewed and approved the final manuscript.

Funding
This study was supported by Natural Science Foundation of Fujian Province (No.2023J01179) and the Joint Funds for the Innovation of Science and Technology, Fujian Province (No. 2021Y9108 & 2023Y9033) and Beijing Xisike Zai Lab Oncology Research Foundation (No. Y-zai2022/qn-0070) and Foundation Sponsored by Fujian Medical University Cancer Hospital, Fujian Cancer Hospital (Grant No: 202412009, to QY. Yue).

Data availability
The data that support the findings of this study are available from the corresponding authors, but restrictions apply to the availability of these data, which were used under license for the current study, and so are not publicly available. Data are however available from the authors upon reasonable request.

Declarations

Ethics approval and consent to participate
The study was performed in accordance with the ethical standards as laid down in the 1964 Declaration of Helsinki and its later amendments or comparable ethical standards. It's approved by the Hospital Ethics Association (Ethics number: [2021] No. 090, the First Affiliated Hospital of Fujian Medical University). Patient anonymity was preserved, and informed consent was exempted in this retrospective study.

Consent for publication
Not applicable.

Competing interests
The authors declare no competing interests.

Author details
[1]Department of Radiology, The First Affiliated Hospital of Fujian Medical University, Fuzhou 350004, China
[2]Department of Radiotherapy, The First Affiliated Hospital of Fujian Medical University, Fuzhou 350004, China
[3]Department of Radiology, Fujian Cancer Hospital & Fujian Medical University Cancer Hospital, Fuzhou 350004, China
[4]Department of Breast Surgery, The Third Affiliated Hospital of Soochow University, Changzhou 213000, China
[5]Department of Radiology, The Third Affiliated Hospital of Soochow University, Changzhou 213000, China
[6]Key Laboratory of Radiation Biology of Fujian Higher Education Institutions, The First Affiliated Hospital, Fujian Medical University, Fuzhou 350004, China
[7]Key Laboratory of Child Development and Learning Science of Ministry of Education, School of Biological Science and Medical Engineering, Southeast University, Nanjing 210096, China
[8]Department of Radiology, National Regional Medical Center, Binhai Campus of the First Affiliated Hospital of Fujian Medical University, Fuzhou 350212, China

Received: 10 March 2024 / Accepted: 5 November 2024
Published online: 11 November 2024

References

1. Siegel RL, Miller KD, Wagle NS, Jemal A: Cancer statistics, 2023. CA Cancer J Clin 2023, 73(1):17–48.
2. Sun Q, Chen Y, Liang C, Zhao Y, Lv X, Zou Y, Yan K, Zheng H, Liang D, Li Z-C: Biologic Pathways Underlying Prognostic Radiomics Phenotypes from Paired MRI and RNA Sequencing in Glioblastoma. Radiology 2021, 301(3):654–663.
3. Yan J, Liu L, Wang W, Zhao Y, Li KK-W, Li K, Wang L, Yuan B, Geng H, Zhang S et al: Radiomic Features From Multi-Parameter MRI Combined With Clinical Parameters Predict Molecular Subgroups in Patients With Medulloblastoma. Front Oncol 2020, 10:558162.
4. van Geel JJL, Boers J, Elias SG, Glaudemans AWJM, de Vries EFJ, Hospers GAP, van Kruchten M, Kuip EJM, Jager A, Menke-van der Houven van Oordt WC et al: Clinical Validity of 16α-[F]Fluoro-17β-Estradiol Positron Emission Tomography/Computed Tomography to Assess Estrogen Receptor Status in Newly Diagnosed Metastatic Breast Cancer. J Clin Oncol 2022:JCO2200400.
5. Choi YS, Ahn SS, Chang JH, Kang S-G, Kim EH, Kim SH, Jain R, Lee S-K: Machine learning and radiomic phenotyping of lower grade gliomas: improving survival prediction. Eur Radiol 2020, 30(7):3834–3842.
6. Duan J, Zhao Y, Sun Q, Liang D, Liu Z, Chen X, Li Z-C: Imaging-proteomic analysis for prediction of neoadjuvant chemotherapy responses in patients with breast cancer. Cancer Med 2023, 12(23):21256–21269.
7. Tsvetkov P, Coy S, Petrova B, Dreishpoon M, Verma A, Abdusamad M, Rossen J, Joesch-Cohen L, Humeidi R, Spangler RD et al: Copper induces cell death by targeting lipoylated TCA cycle proteins. Science 2022, 375(6586):1254–1261.
8. Yan C, Han Z, Chen X, Gao L, Ye R, Li Y: Diffusion-Weighted Imaging as a Quantitative Imaging Biomarker for Predicting Proliferation Rate in Hepatocellular Carcinoma: Developing a Radiomics Nomogram. J Comput Assist Tomogr 2023, 47(4):539–547.
9. Hong F, Meng Q, Zhang W, Zheng R, Li X, Cheng T, Hu D, Gao X: Single-Cell Analysis of the Pan-Cancer Immune Microenvironment and scTIME Portal. Cancer Immunol Res 2021, 9(8):939–951.
10. Hu JF, Song X, Zhong K, Zhao XK, Zhou FY, Xu RH, Li JL, Wang XZ, Li XM, Wang PP et al: Increases prognostic value of clinical-pathological nomogram in patients with esophageal squamous cell carcinoma. Front Oncol 2023, 13:997776.
11. Dogan S, Vasudevaraja V, Xu B, Serrano J, Ptashkin RN, Jung HJ, Chiang S, Jungbluth AA, Cohen MA, Ganly I et al: DNA methylation-based classification of sinonasal undifferentiated carcinoma. Mod Pathol 2019, 32(10):1447–1459.
12. Hanahan D: Hallmarks of Cancer: New Dimensions. Cancer Discov 2022, 12(1):31–46.
13. Khouja HI, Ashankyty IM, Bajrai LH, Kumar PKP, Kamal MA, Firoz A, Mobashir M: Multi-staged gene expression profiling reveals potential genes and the critical pathways in kidney cancer. Sci Rep 2022, 12(1):7240.
14. Zhang J, Kong X, Zhang Y, Sun W, Wang J, Chen M, Chen X: FDXR regulates TP73 tumor suppressor via IRP2 to modulate aging and tumor suppression. J Pathol 2020, 251(3):284–296.
15. García-Heredia JM, Carnero A: Role of Mitochondria in Cancer Stem Cell Resistance. Cells 2020, 9(7).
16. Hsu C-C, Tseng L-M, Lee H-C: Role of mitochondrial dysfunction in cancer progression. Exp Biol Med (Maywood) 2016, 241(12):1281–1295.
17. Ping Y, Shan J, Qin H, Li F, Qu J, Guo R, Han D, Jing W, Liu Y, Liu J et al: PD-1 signaling limits expression of phospholipid phosphatase 1 and promotes intratumoral CD8 + T cell ferroptosis. Immunity 2024, 57(9).
18. Lambin P, Leijenaar RTH, Deist TM, Peerlings J, de Jong EEC, van Timmeren J, Sanduleanu S, Larue RTHM, Even AJG, Jochems A et al: Radiomics: the bridge between medical imaging and personalized medicine. Nat Rev Clin Oncol 2017, 14(12):749–762.
19. Yan J, Zhao Y, Chen Y, Wang W, Duan W, Wang L, Zhang S, Ding T, Liu L, Sun Q et al: Deep learning features from diffusion tensor imaging improve glioma stratification and identify risk groups with distinct molecular pathway activities. EBioMedicine 2021, 72:103583.
20. Zhao Y, Liu G, Sun Q, Zhai G, Wu G, Li Z-C: Validation of CT radiomics for prediction of distant metastasis after surgical resection in patients with clear cell renal cell carcinoma: exploring the underlying signaling pathways. Eur Radiol 2021, 31(7):5032–5040.
21. Yan J, Sun Q, Tan X, Liang C, Bai H, Duan W, Mu T, Guo Y, Qiu Y, Wang W et al: Image-based deep learning identifies glioblastoma risk groups with genomic and transcriptomic heterogeneity: a multi-center study. Eur Radiol 2023, 33(2):904–914.
22. Rossi G, Barabino E, Fedeli A, Ficarra G, Coco S, Russo A, Adamo V, Buemi F, Zullo L, Dono M et al: Radiomic Detection of EGFR Mutations in NSCLC. Cancer Res 2021, 81(3):724–731.

23. Bi S, Li J, Wang T, Man F, Zhang P, Hou F, Wang H, Hao D: Multi-parametric MRI-based radiomics signature for preoperative prediction of Ki-67 proliferation status in sinonasal malignancies: a two-centre study. Eur Radiol 2022.
24. Zhang Q-W, Gao Y-J, Zhang R-Y, Zhou X-X, Chen S-L, Zhang Y, Liu Q, Xu J-R, Ge Z-Z: Personalized CT-based radiomics nomogram preoperative predicting Ki-67 expression in gastrointestinal stromal tumors: a multicenter development and validation cohort. Clin Transl Med 2020, 9(1):12.
25. Li Z-Y, Wang X-D, Li M, Liu X-J, Ye Z, Song B, Yuan F, Yuan Y, Xia C-C, Zhang X et al: Multi-modal radiomics model to predict treatment response to neoadjuvant chemotherapy for locally advanced rectal cancer. World J Gastroenterol 2020, 26(19):2388–2402.
26. Pai S, Bontempi D, Prudente V, Hadzic I, Sokač M, Chaunzwa TL, Bernatz S, Hosny A, Mak RH, Birkbak NJ et al: Foundation Models for Quantitative Biomarker Discovery in Cancer Imaging. medRxiv 2023.
27. Wu J, Li C, Gensheimer M, Padda S, Kato F, Shirato H, Wei Y, Schönlieb C-B, Price SJ, Jaffray D et al: Radiological tumor classification across imaging modality and histology. Nat Mach Intell 2021, 3:787–798.
28. Braman N, Prasanna P, Whitney J, Singh S, Beig N, Etesami M, Bates DDB, Gallagher K, Bloch BN, Vulchi M et al: Association of Peritumoral Radiomics With Tumor Biology and Pathologic Response to Preoperative Targeted Therapy for HER2 (ERBB2)-Positive Breast Cancer. JAMA Netw Open 2019, 2(4):e192561.
29. Li Z-C, Bai H, Sun Q, Zhao Y, Lv Y, Zhou J, Liang C, Chen Y, Liang D, Zheng H: Multiregional radiomics profiling from multiparametric MRI: Identifying an imaging predictor of IDH1 mutation status in glioblastoma. Cancer Med 2018, 7(12):5999–6009.
30. Sun R, Limkin EJ, Vakalopoulou M, Dercle L, Champiat S, Han SR, Verlingue L, Brandao D, Lancia A, Ammari S et al: A radiomics approach to assess tumour-infiltrating CD8 cells and response to anti-PD-1 or anti-PD-L1 immunotherapy: an imaging biomarker, retrospective multicohort study. Lancet Oncol 2018, 19(9):1180–1191.
31. Li H, Zhu Y, Burnside ES, Drukker K, Hoadley KA, Fan C, Conzen SD, Whitman GJ, Sutton EJ, Net JM et al: MR Imaging Radiomics Signatures for Predicting the Risk of Breast Cancer Recurrence as Given by Research Versions of MammaPrint, Oncotype DX, and PAM50 Gene Assays. Radiology 2016, 281(2):382–391.
32. Bao H, Chen T, Zhu J, Xie H, Chen F: CEUS-Based Radiomics Can Show Changes in Protein Levels in Liver Metastases After Incomplete Thermal Ablation. Front Oncol 2021, 11:694102.
33. Grossmann P, Gutman DA, Dunn WD, Holder CA, Aerts HJWL: Imaging-genomics reveals driving pathways of MRI derived volumetric tumor phenotype features in Glioblastoma. BMC Cancer 2016, 16:611.
34. Katsoulakis E, Yu Y, Apte AP, Leeman JE, Katabi N, Morris L, Deasy JO, Chan TA, Lee NY, Riaz N et al: Radiomic analysis identifies tumor subtypes associated with distinct molecular and microenvironmental factors in head and neck squamous cell carcinoma. Oral Oncol 2020, 110:104877.

Publisher's note

Springer Nature remains neutral with regard to jurisdictional claims in published maps and institutional affiliations.